A SUMMARY OF THE WORKSHOP ON NEUTRON SCATTERING DATA ANALYSIS HELD AT THE RUTHERFORD APPLETON LABORATORY IN MARCH 1990

M W Johnson

Rutherford Appleton Laboratory, Chilton, Didcot, Oxon, OX11 0QX, UK

The workshop on neutron scattering data analysis, held at the Rutherford Appleton Laboratory in March 1990, included 22 presentations, 21 of which are included in the IOP Conference Series No 107 to be published in November 1990. Table 1 lists the contributions and their authors. In a talk of this length is is obviously impossible to mention them all, and I have therefore made a personal selection, highlighting those talks which will be of interest to the widest neutron scattering community.

The first is the paper by Ron Ghosh and Adrian Rennie on small angle scattering. They asked the simple question 'Are existing SANS results correct' – bearing in mind the fact that the scattering is assumed to be elastic when it often clearly is not. They answered this question by introducing time-of-flight analysis onto the D17 instrument at the ILL. Figure 1 shows the SANS patterns for perdeuterated polystyrene (PS-d) in hydrogenous toluene, at a series of time-of-flight. The inelastic contribution is quite clear. Analysis using just the elastic channels, Figure 2a, and the total scattering, Figure 2b, show small, but significant, differences. For example, the derived radius of gyration is 24.7Å (elastic scattering) whereas the conventional analysis from the totally scattered neutrons gave 25.9Å. The authors were able to show that, in this example, despite the considerable thermalisation in the sample, the subtraction of the background toluene pattern largely removes the inelastic effects, resulting in substantially correct results. Although only a few percent error is introduced in this example, the authors point out that for models involving greater weight at high Q (Porod's Law) or Fourier transforms the results could be substantially worse.

In reflectometry we had two complementary contributions. Jeff Penfold presented the 'classical' approach of model fitting, illustrating the method with simple examples. Figure 3a shows data from a single 'perfect' surface well fitted by the Fresnel law; 3b shows a 48 layer Langmuir Blodgett film modelled by a single uniform layer of 1186Å with roughness of 20Å at the air-film and film-substrate interfaces; 3c shows that at higher Q a 20 layer Langmuir Blodgett film requires the specific inclusion of the bilayer structure to include the Bragg peak observed at 0.12 Å⁻¹.

Davinda Sivia presented some MaxEnt results in which the density profile $\beta(z)$ (β is the average neutron scattering length density, z = depth below surface) is determined by inverting the data using the MaxEnt formulism. A number of striking successes were presented (Figures 4, 5 and 6), which also illustrated the insensitivity of the data to translation (i.e. $\beta(z+a) = \beta(z)$) or inversion $\beta(-z) = \beta(z)$. A clear example was also given of the technique producing quite the wrong answer (Figure 7) which should act as a cautionary note. However, this example was retrieved when further information was supplied (Figure 8). Clearly this method shows promise – but also some additional work in establishing the confidence levels one can place in the result.

In liquids and amorphous diffraction the session was treated to a 'live display' of data analysis using the Reverse Monte Carlo (RMC) technique by Bob McGreevy. In standard Monte Carlo methods, atomic or molecular configurations are determined by minimising an energy cost function, subject to certain constraints, using a weighted sampling procedure. In this case the 'cost function' is derived from theoretical interaction potentials. In RMC the ensemble of atoms

is modified with the aim of reducing χ^2 until it reaches 1. The 'cost function' is now the disagreement between model and observed data. The beauty of the technique lies in its ability to combine different types of data into the analysis. Figure 9 shows the fit of an atomic ensemble to both the X-ray and neutron structure factors for vitreous silica. From this model it is then possible to calculate **three** partial radial distribution functions - from only two measurements! In addition, RMS produces a 3-d structure from which broad angle distributions may be calculated (Figure 10).

Another problem tackled by RMC is liquid sulphur - is the structure based on rings, chains or a mixture, and what happens at the viscous transition? RMC fitting to the structure factor at 423 and 503K (either side of the transition) gives a structure of entangled, broken chains. The average coordination is close to 2, although this comes from 40% 2-coordination + 40% 1 or 3 coordination. The interesting point is that with RMC the model may be constrained - and doing this to produce 92% 2-coordination led to results equally consistent with the data. Examples of high and low 2 coordination are shown in Figure 11.

The crystallographic section of the meeting also produced two excellent presentations on the use of MaxEnt methods. In the first, Papoular and Gillon showed how the limited data from polarised neutron diffraction data may be inverted successfully to determine magnetic structures. In a model example (Figure 12) two positive and two negative magnetic moments are used in a 2-d example. Figures 12a, 12b and 12c show standard Fourier transforms using increasing numbers of reflections, the ME reconstruction (Figure 12d) eliminates truncation effects and quite clearly exhibits the two small negative moments. In a 'real data' case the chemical bonding in tanol suberate was examined. Figure 13 shows the results. Standard Fourier analysis does not resolve the electronic density about the NO group (Figures 13a, 13c) whereas the ME procedure yields clearly resolved features (Figures 13b, 13d) and moreover gives a good value of 3.7 μB for the average magnetisation per unit cell again 3.2 $\pm$ μB obtained from independent, macroscopic measurements.

Another use of ME in crystallography has produced outstanding results. A paper by Bill David (RAL) described how excellent Patterson maps may be obtained using the MaxEnt technique and the results shown to be correct. David has used experimental data from rutile (TiO_2) recorded on the POLARIS spectrometer at ISIS (Figure 14). Using conventional equipartition of overlapping powder lines and Fourier inversion, the maps shown in Figures 15a, 15b and 15c are obtained. Using the criterion of maximising 'Patterson Entropy', the maps in Figures15d, 15e and 15f are obtained - which are certainly sharper. These are not only sharper - but correct - since these Patterson peaks are in excellent agreement with the known interatomic vectors. Confirmation of the validity of the method is also provided by a back-calculation of individual structure factors to obtain a R-factor for the two methods :

$$R_{EQ} = 34\%$$
$$R_{ME} = 14\%$$

This method also holds great promise as the first stage in structure determinations based on Patterson inversions.

In the section on general techniques the meeting was given an excellent review of the subject of simulated annealing. As its name implies, the method attempts to mimic the solidification or annealing process that occurs in solid-liquid transitions to obtain a global minimisation to optimisation problems. The applications are vast ranging from the mathematical (travelling

salesman problems) to engineering (VSLI placement and routing problems) and scientific (structure determination). In fact, the method has been used in a similar way to RMC (which it proceeded) to solve structures directly by minimising the R-factor. More dramatically, it has also been used to determine zeolite crystal structures from crystal-chemistry rules alone.

Finally, two papers on MaxEnt pointed to new future directions in the field. The one by John Skilling introduced the subject to non-experts - but also alluded to the new work on confidence intervals that may be calculated using ME. This new software - MEMSYS III - provides this facility, and this should help make the technique more widely acceptable to the scientific community at large.

The second of these two papers was by Alan Soper (RAL) who dared to raise the question as to whether the ME criterion, while powerful, was sufficient in certain circumstances. He notes the difficulties of ME in inverting certain problems (especially the $S(Q) \rightarrow g(r)$ inversion) and the fact that apparently "noisy" solutions can have the same entropy as 'smooth' solutions, see for example Figure 16.

I would like to conclude with some remarks of my own which were not made at the WONSDA meeting. I believe that the MaxEnt method, at its roots, is perfectly sound - the problem is that the theory has been developed for probability distributions and has been applied without sufficient questioning to spectra. Spectra have some of the attributes of probability distributions, but are not identical. It is in some ways a tribute to the ME method that it has worked so well for spectra.

To illustrate the point I show Figure 17. The data are crosses and two possible 'solutions' are shown by the dotted or dashed lines. Both of these lines have the same χ^2 and entropy, and hence would be equally acceptable to a ME algorithm. The point about a spectrum is that it is an **ordered** series of values, whereas a probability distribution is not. Hence the ME criterion cannot distinguish one solution from another. However, Bayes Theorem has the power to allow us to include a 'desirability' (from Occam's Razor) criterion within the prior to enable these distinctions to be made. Some work now has to be done on the mathematical formulation of Occam's Razor, and its inclusion into a Bayesian/ME formalism.

|	
J Pannetier*	Simulated Annealing: an introduction and a few applications to problems of structure determination
R L McGreevy	Reverse Monte Carlo (RMC) simulation: modelling disordered structures from diffraction data
D A Keen	Determining structural disorder in crystalline materials by Reverse Monte Carlo (RMC) simulation
P Wolfers	MXD: A general least-squares program for non-standard crystallographic refinements
R P Piltz	On the normalization of spallation-source powder diffraction data
M Anne	Real-time neutron powder diffraction study of $MoO_3.2H_2O$ Topotactic Dehydration
C C Wilson	Data analysis of reciprocal space volumes
J Skilling*	Quantified maximum entropy data processing
R J Papoular	Maximum entropy reconstruction of spin density maps in crystals from polarised neutron diffraction data
W I F David	Unscrambling powder diffraction data
D S Sivia	The Bayesian approach to optimal instrument design
A K Soper	An amateur's guide to the pitfalls of maximum entropy – or – a practical solution to two well-known problems in linear inversion of experimental data
M J D Powell*	Radial basis function methods for multivariable approximation
A Smith	Analysis of quasielastic and inelastic scattering data from crystal analyser instruments
H Tietze	Computational aspects in scan performance of the Rotating Analyser Crystal Spectrometer ROTAX
A C Hannon	ATLAS – A package of routines for the analysis of time-of-flight diffraction data from liquid and amorphous samples
F Cilloco	A normalization procedure of liquid diffraction data based on the knowledge of the sample neutron cross section
K M Crennell	NUVU, a program for the visualisation of neutron scattering data based on UNIRAS
C-K Loong*	S(Q,E) analysis for chopper spectrometer data
R Osborn	Multi-phonon and multiple scattering corrections to $S(Q,\omega)$
G J Kearley	CLIMAX – recent extensions
J Penfold*	Analysis of neutron reflectivity data using constrained model fitting
D S Sivia	Maximum entropy analysis of reflectivity data – some preliminary results
C Moreton-Smith	GENIE Version 3: A tool for neutron scattering data analysis and visualisation

Table 1

1018
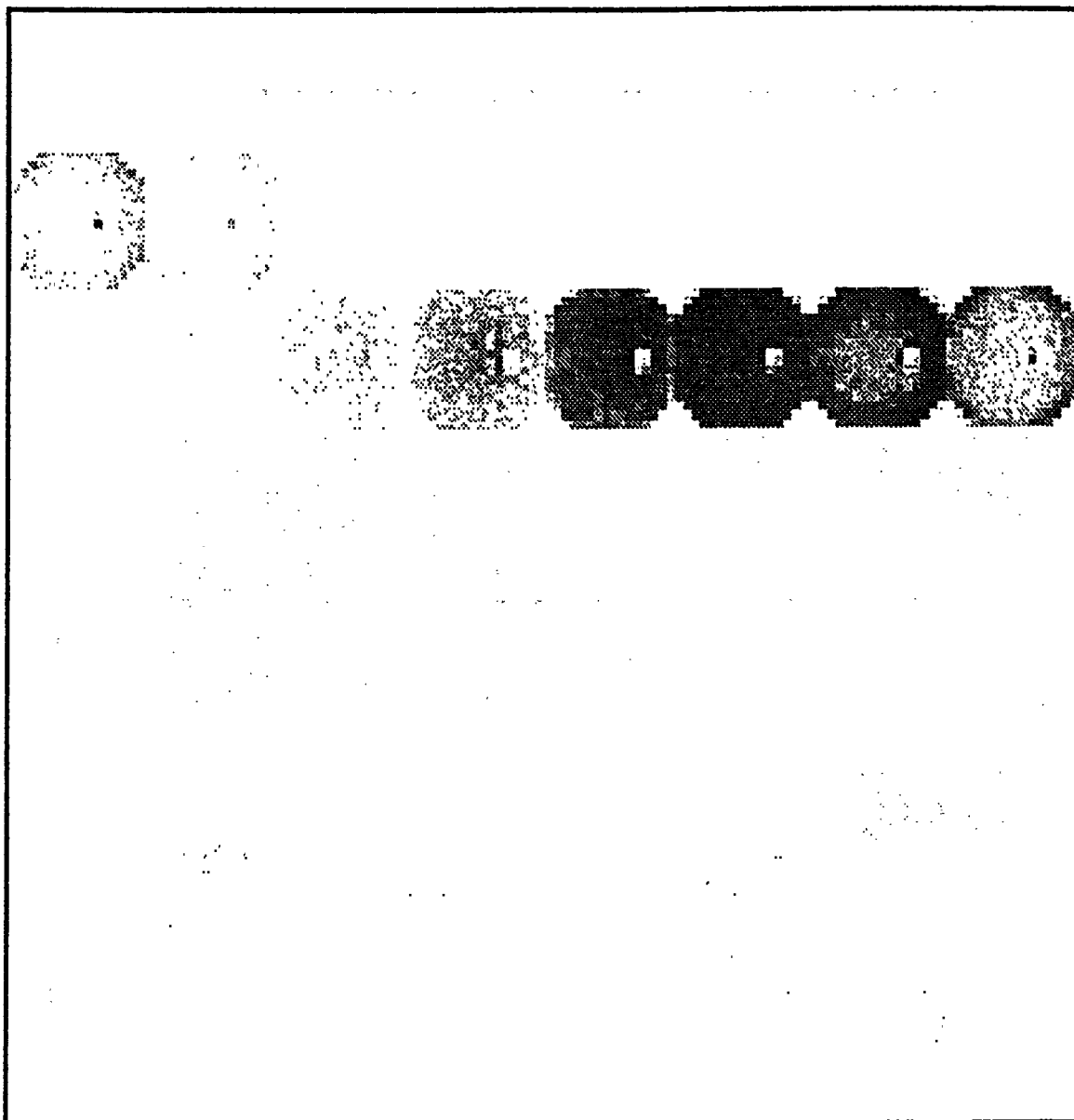
Fig. 1 A set of 64 two-dimensional spectra for 1mm water (25 C) as a function of time-of-flight (raw data). The grey scale goes from light to dark with increasing intensity. The time scale for neutron arrival starts at short times in the bottom left hand corner and increases by rows from left to right and from bottom to top. The most intense signal corresponds to elastic scattering of .12 Å neutrons (time channel 46). The detector is 6 degrees of axis and the beam stop protecting the detector from the incident beam is off-centre showing as a white spot on each frame. The large fraction of inelastically scattered neutrons is evident from the intensity at short times of flight.

(a) I(Q)
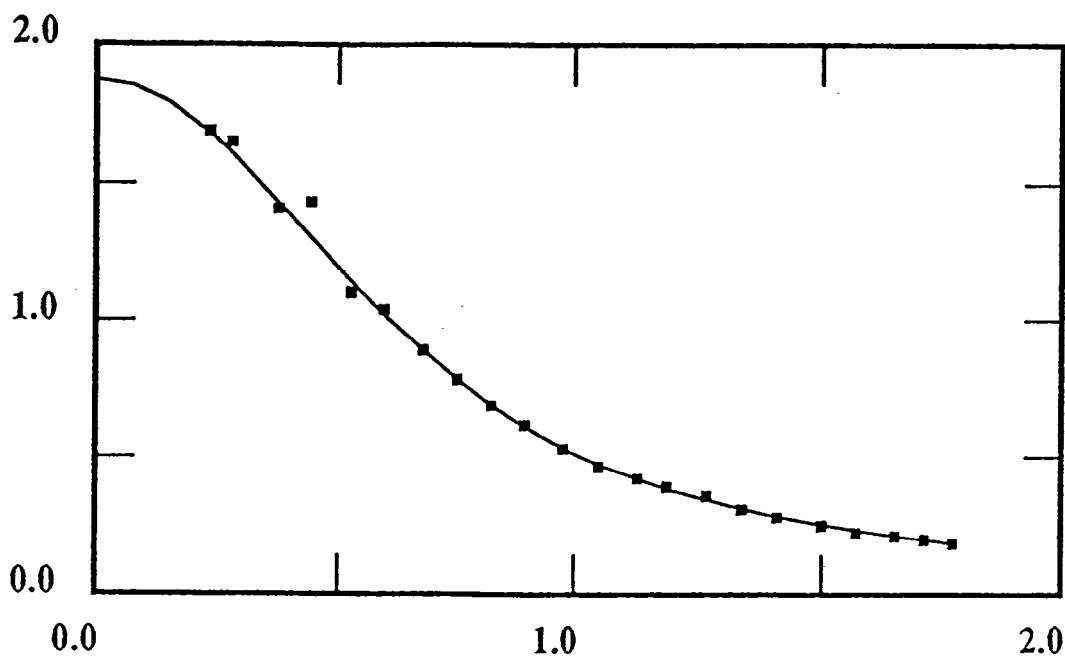
(b) I(Q)
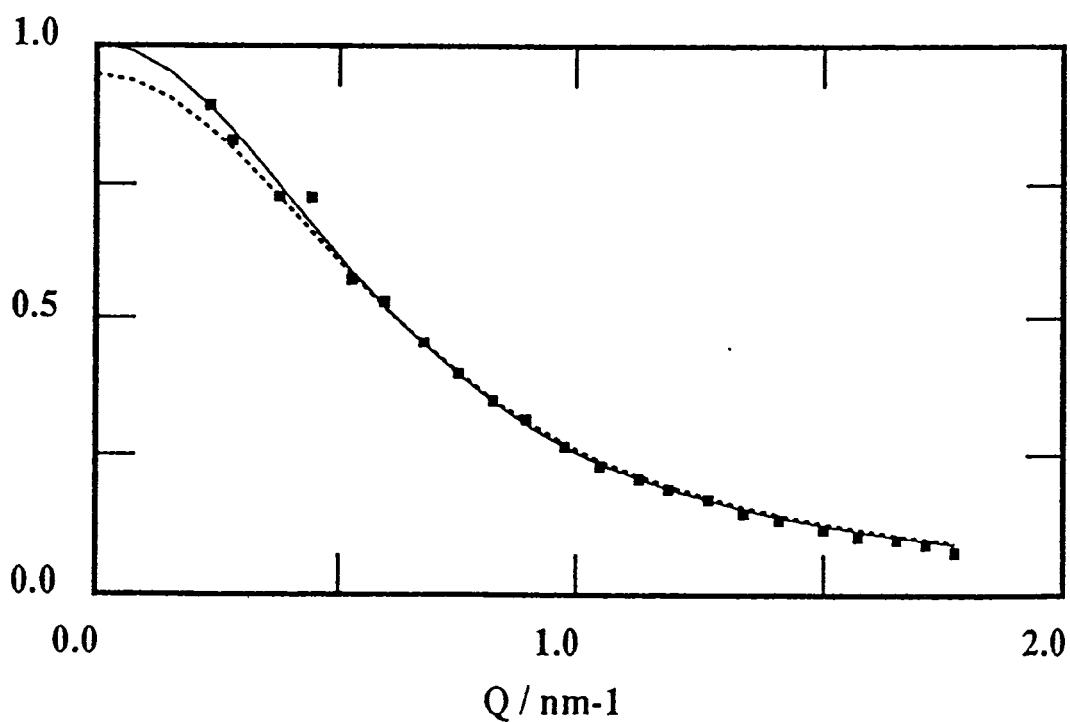
Fig. 2 (a) Elastic scattering for PS-d in toluene with fit of Debye function and (b) total scattering, all time channels, with best fit to data (solid line) and the model fitted to elastic data rescaled (dashes) The latter data show the deviation at large Q values due to an over correction with water.

Reflectivity

Momentum transfer, Q (Å^{-1})

a

Reflectivity

Momentum transfer, Q (Å^{-1})

b

Reflectivity

c

Fig 3

DATA

(a)

Reflectivity

Momentum Transfer Q (A⁻¹)

MaxEnt Reconstruction

(b)

β

Z

Fit to Data

(c)

Reflectivity

Momentum Transfer Q (A⁻¹)

The Object

(d)

β

Z
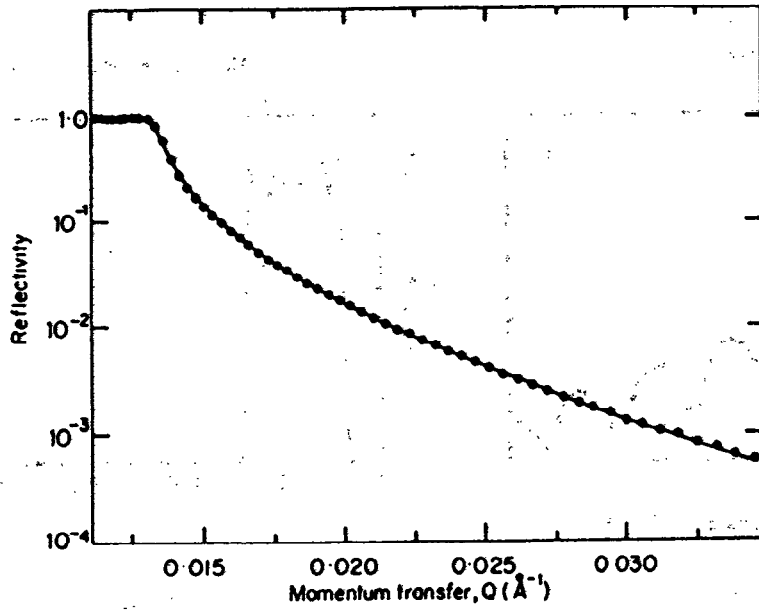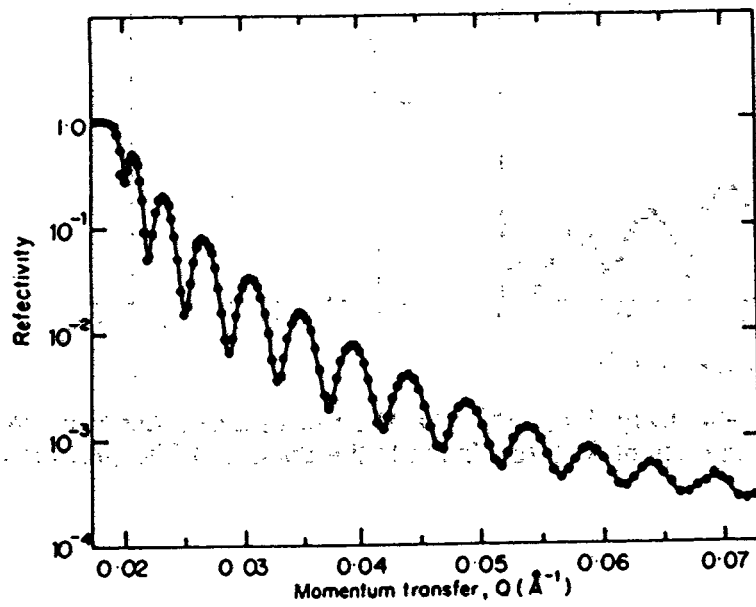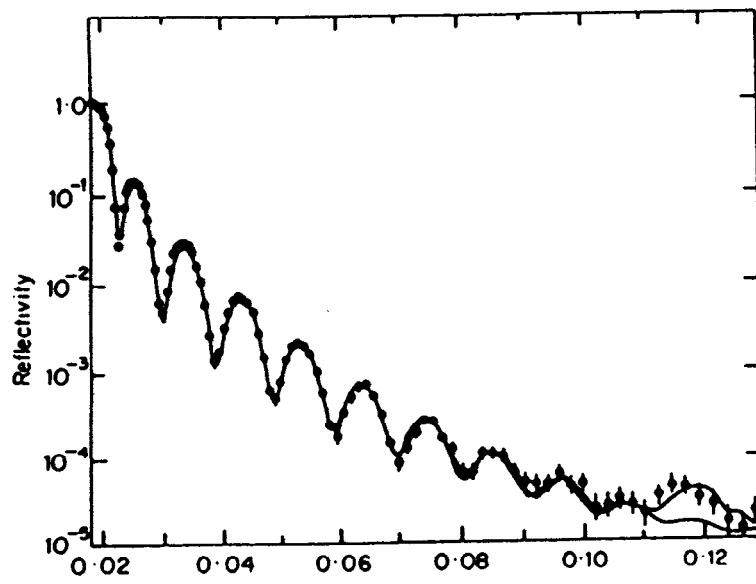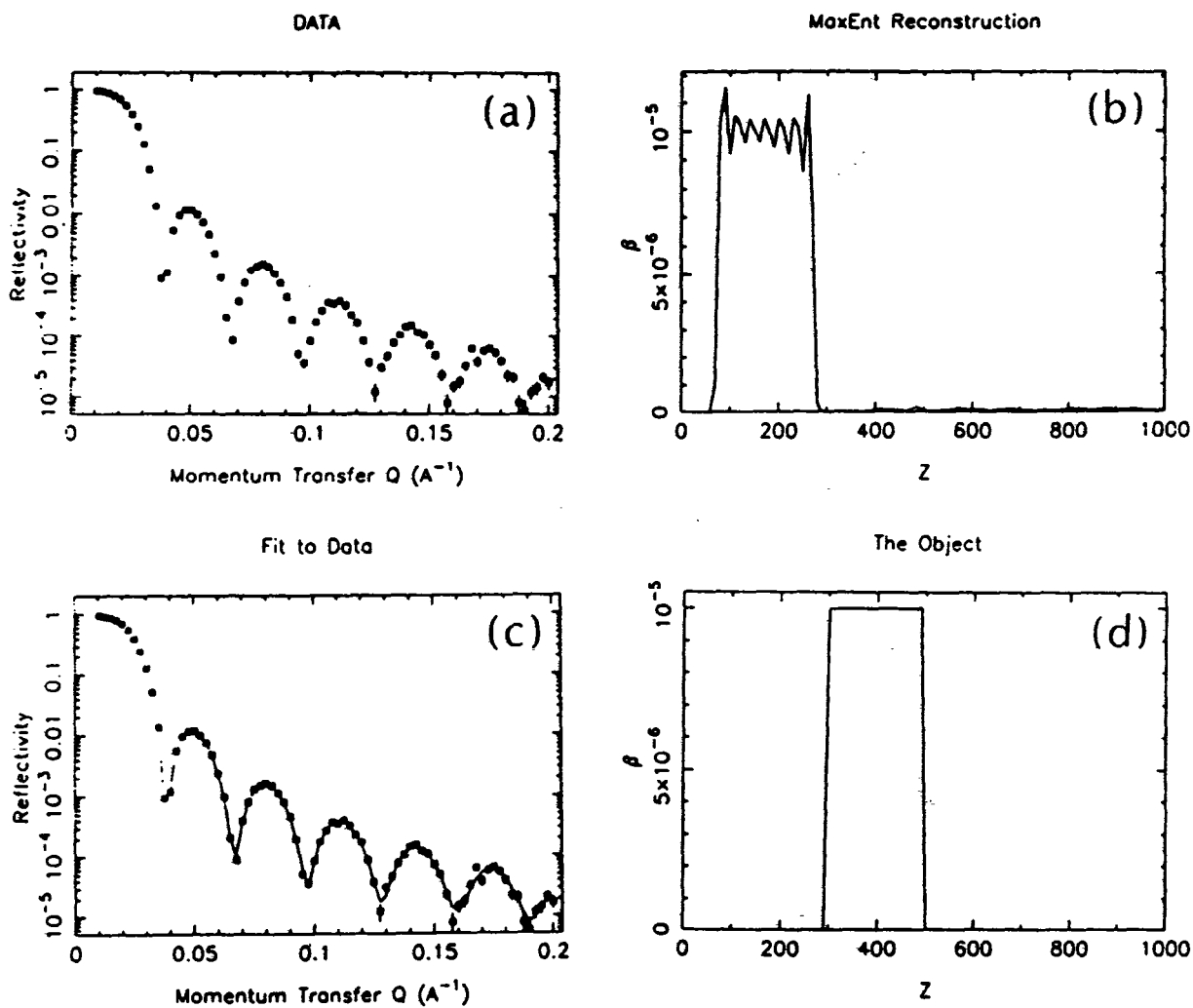
Figure 4 **(a)** Simulated reflectivity data. **(b)** The MaxEnt reconstruction of the depth profile. (z is in units of Å, and β is in units of Å⁻².) **(c)** The fit to the data. **(d)** The (true) test profile.

DATA

(a)

MaxEnt Reconstruction

(b)

Fit to Data

(c)

The Object

(d)
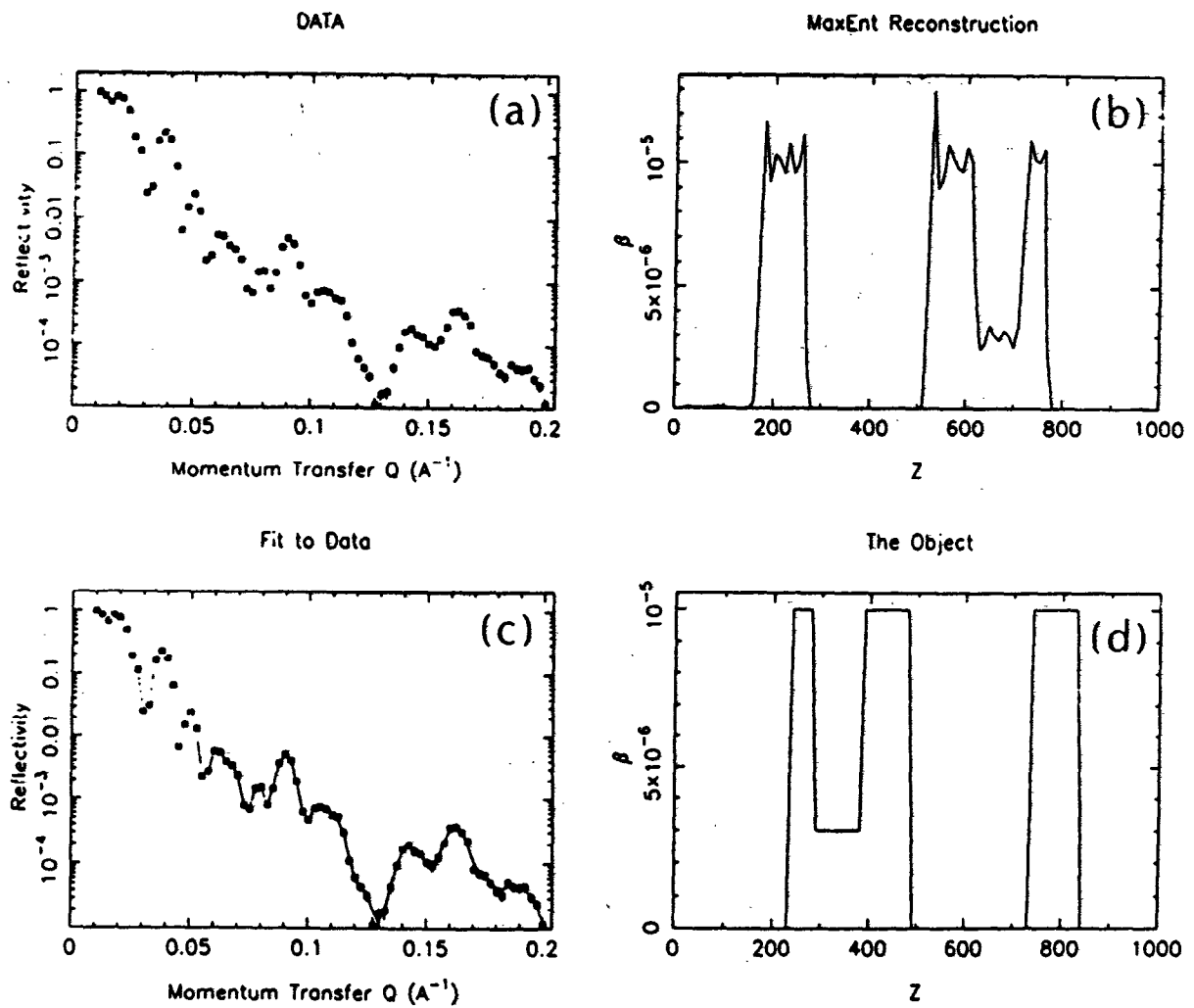
Figure 5 (a) Simulated reflectivity data. (b) The MaxEnt reconstruction of the depth profile. (c) The fit to the data. (d) The test profile.
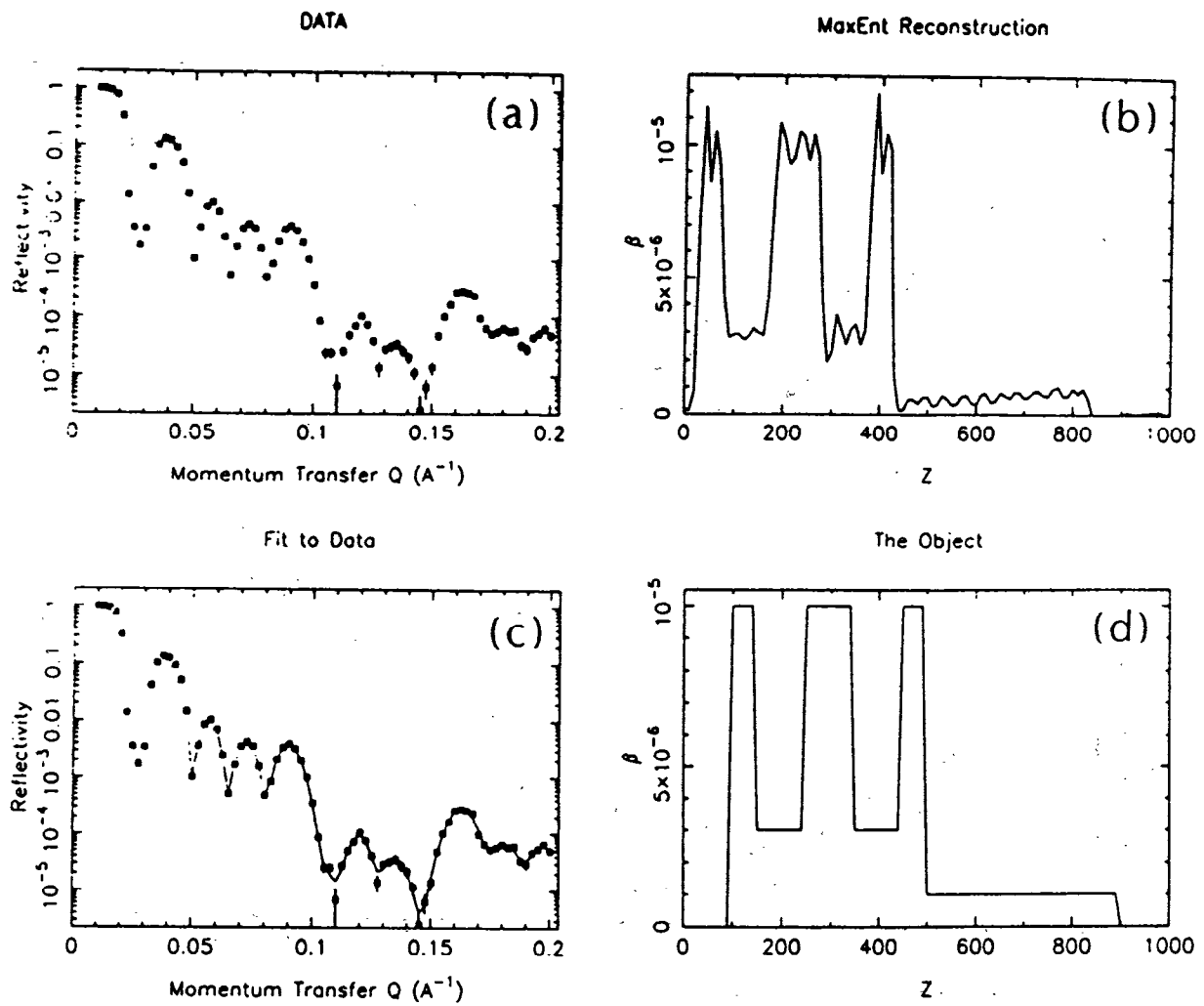
Figure 6 **(a)** Simulated reflectivity data. **(b)** The MaxEnt reconstruction of the depth profile. **(c)** The fit to the data. **(d)** The test profile.

DATA

MaxEnt Reconstruction

(a)

(b)

Momentum Transfer Q (A⁻¹)

Z

Fit to Data

The Object

(c)

(d)

Momentum Transfer Q (A⁻¹)

Z
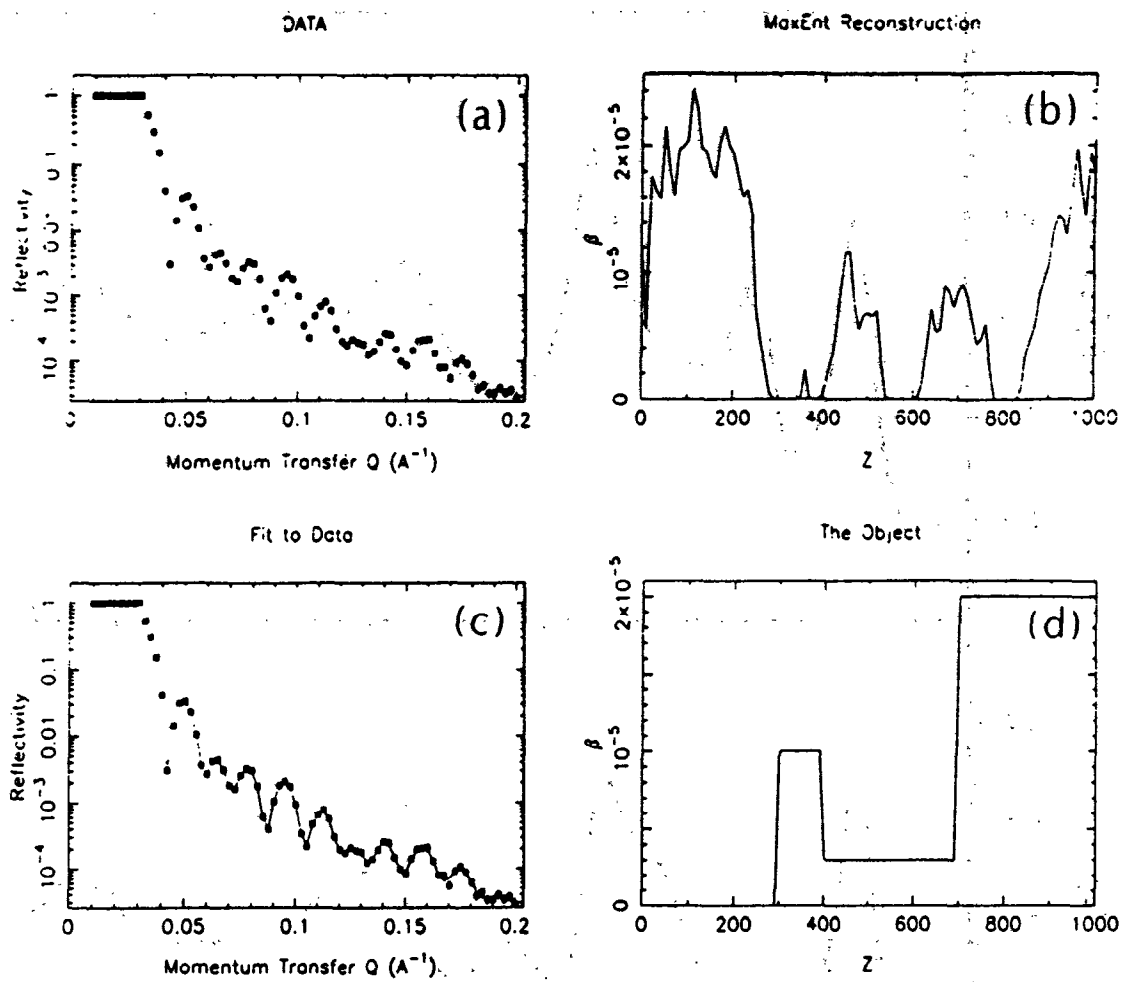
Figure 7 : (a) Simulated reflectivity data. (b) The MaxEnt reconstruction of the depth profile. (c) The fit to the data. (d) The test profile.

MaxEnt Reconstruction

MaxEnt Reconstruction

(a)

(b)

Z

Z
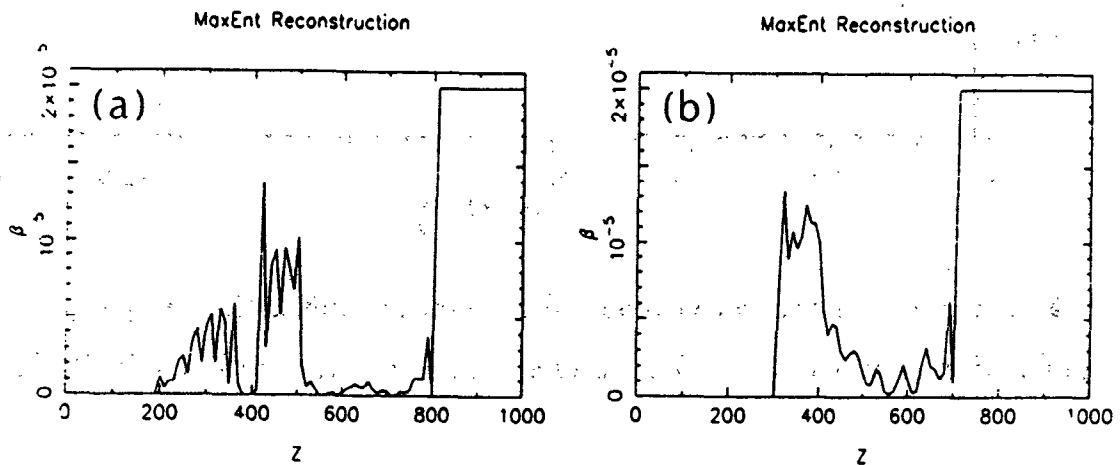
Figure 8 : Analysis of the reflectivity data in Fig. 6(a) using some additional prior knowledge. (a) Given the substrate and that the sample is less than 600Å thick. (b) Given the substrate and that the sample is 400 Å thick.
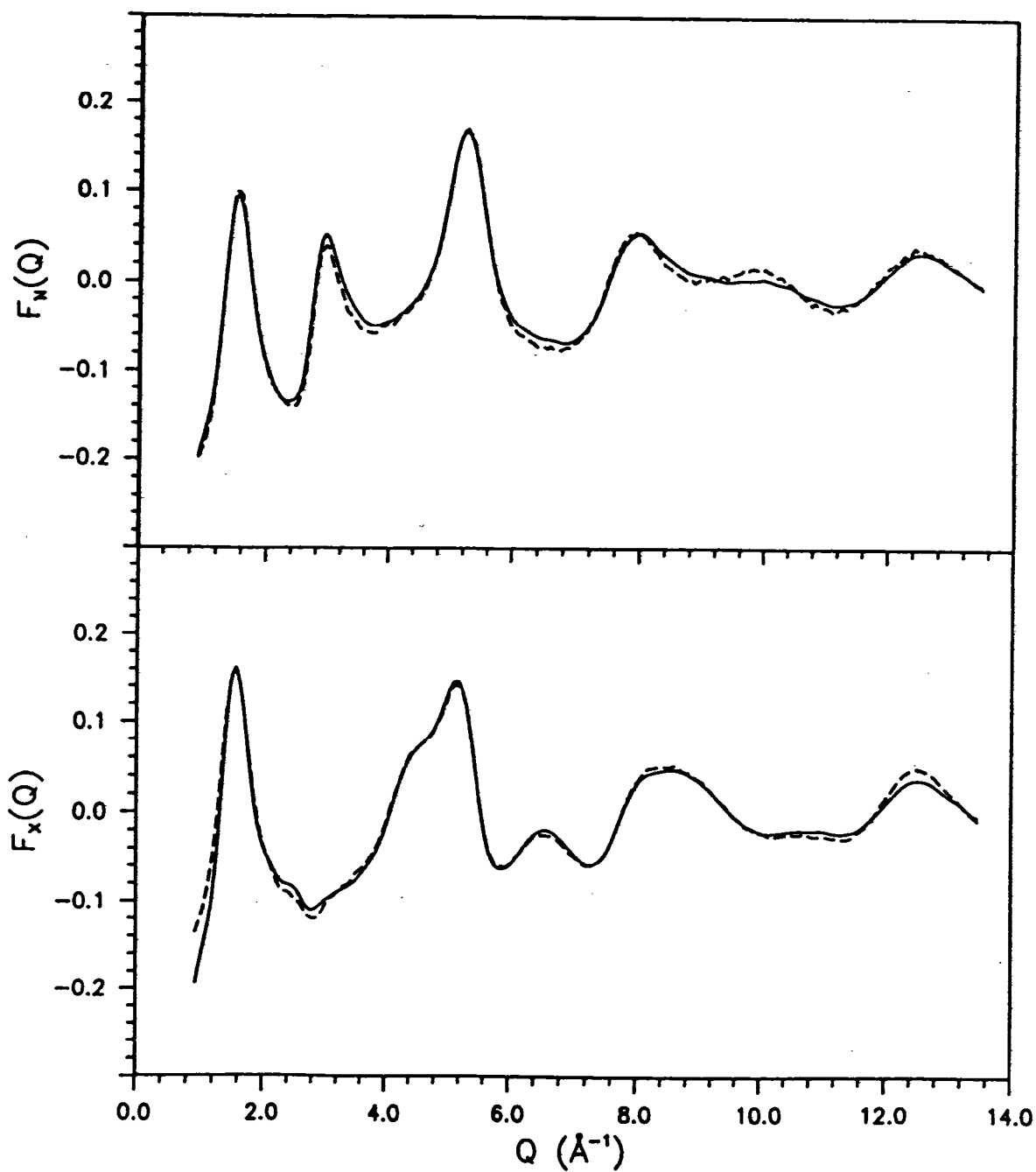
Figure 9. Structure factors for vitreous silica: neutron diffraction (upper graph) and X-ray diffraction (lower graph). Broken line - experiment; solid line - RMC fit.
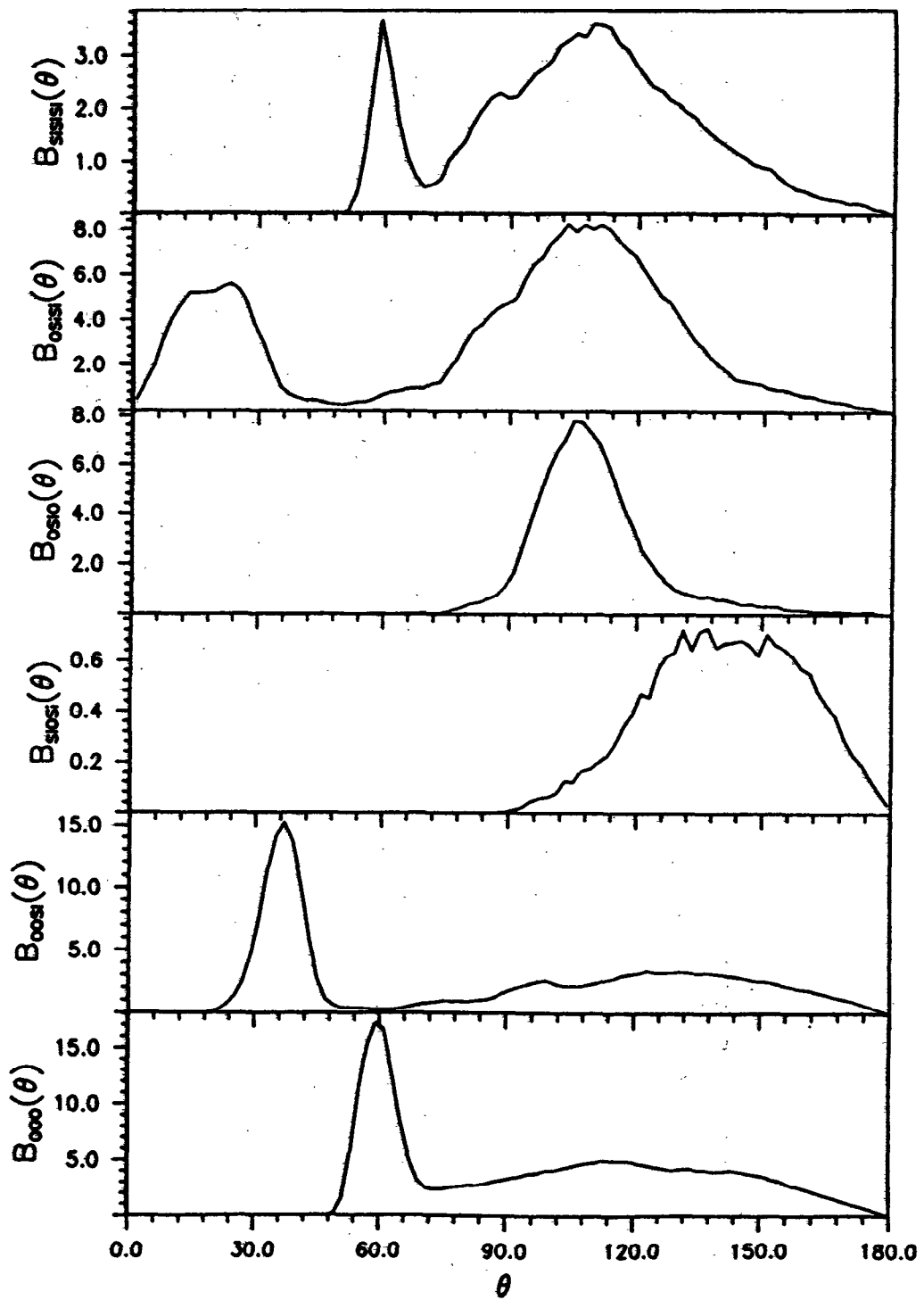
Figure 10 Bond angle distributions for vitreous silica. Maximum bond lengths are defined by the first minima in the appropriate partial radial distribution functions.
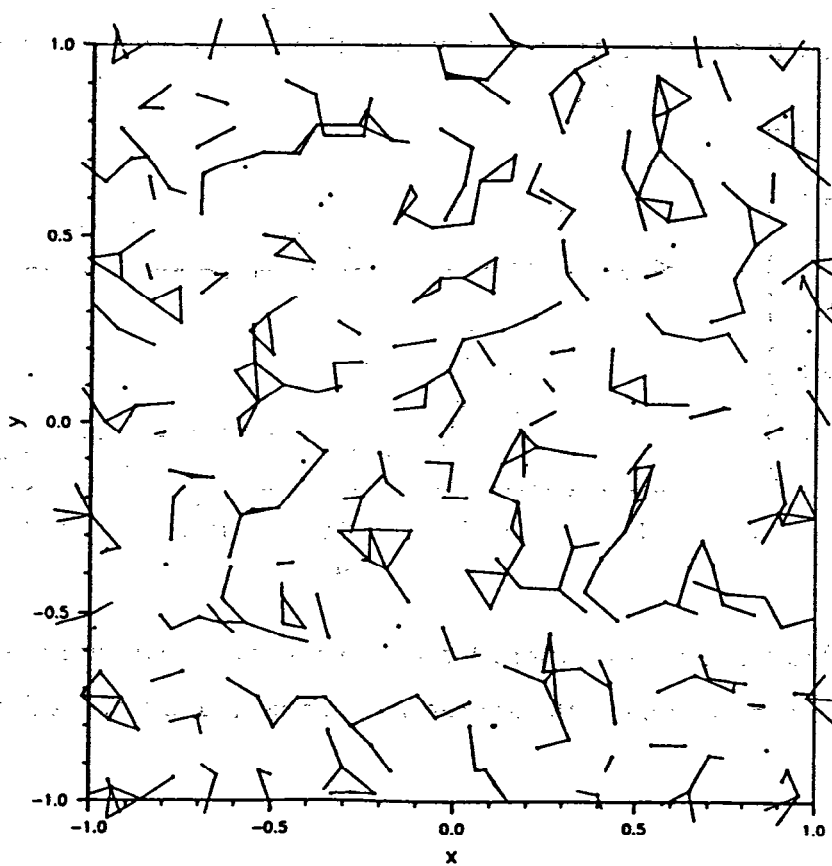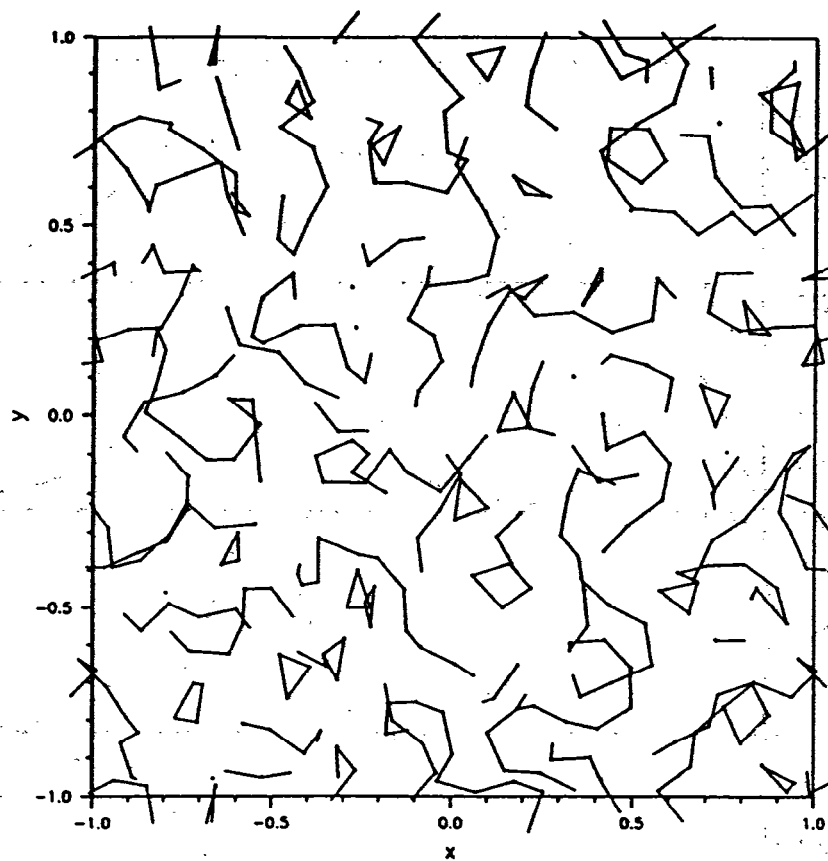
Figure 11 S-S bonds in sections from configurations for liquid sulphur at 423K: high 2-fold coordination (upper graph) and low 2-fold coordination (lower graph).
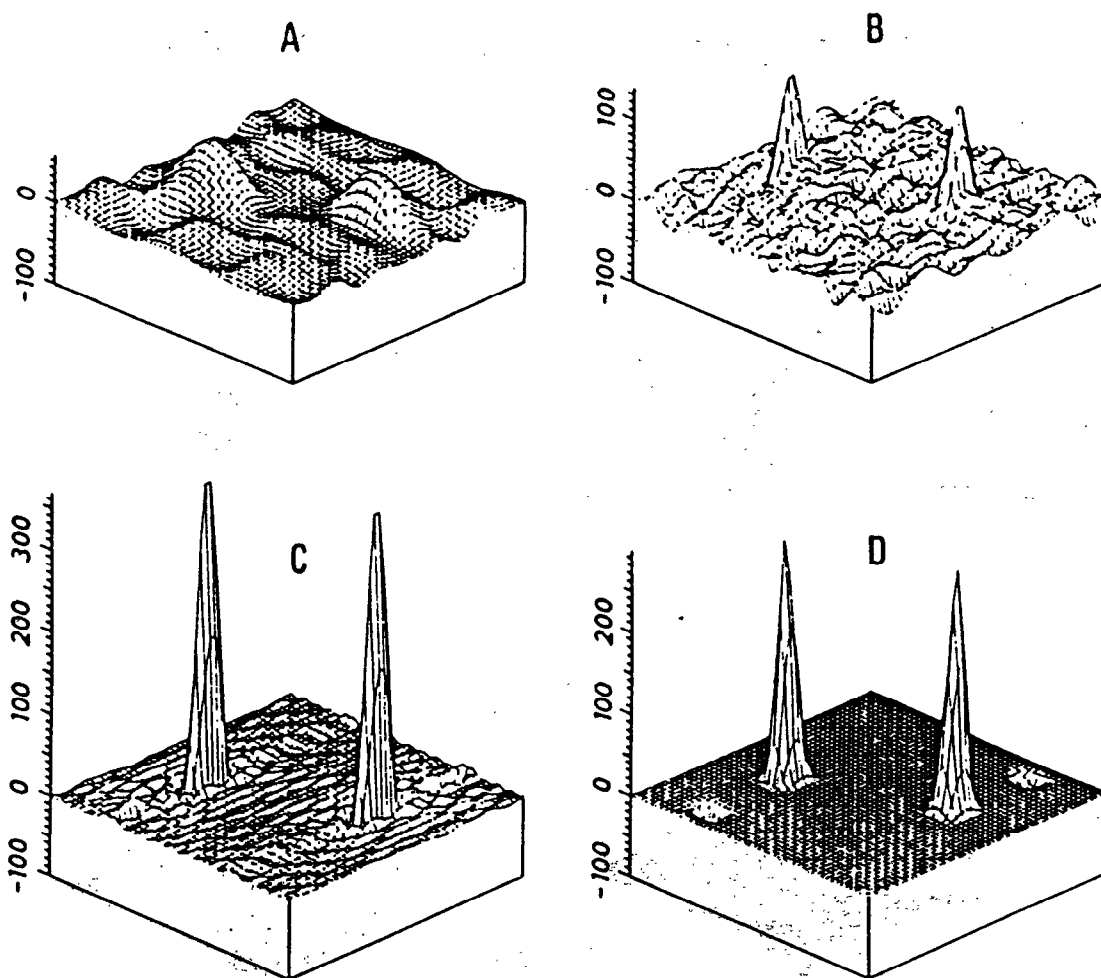
Fig.12 Simulation involving two positive $(+1.25\mu_B)$ and two negative $(-0.25\mu_B)$ magnetic moments. The unit cell is assumed to be orthorhombic, and the only symmetry operations are the Identity and the Inversion. The projection is taken along the $\vec{a}$ crystallographic axis. The reconstructed magnetisation density is expressed in $\mu_B/\mathring{A}^2$. The size of the image is 50*50 pixels.

Orthographic projections in crystallographic units:

A,B,C : straightforward Inverse Fourier transforms for an increasing number of reflections (23,72, and 262 respectively). Using more Fourier components does not eliminate truncation effects.

D: Maximum Entropy reconstruction using the same 23 reflections as in A. Truncation effects have vanished and the two negative features are now clearly apparent.
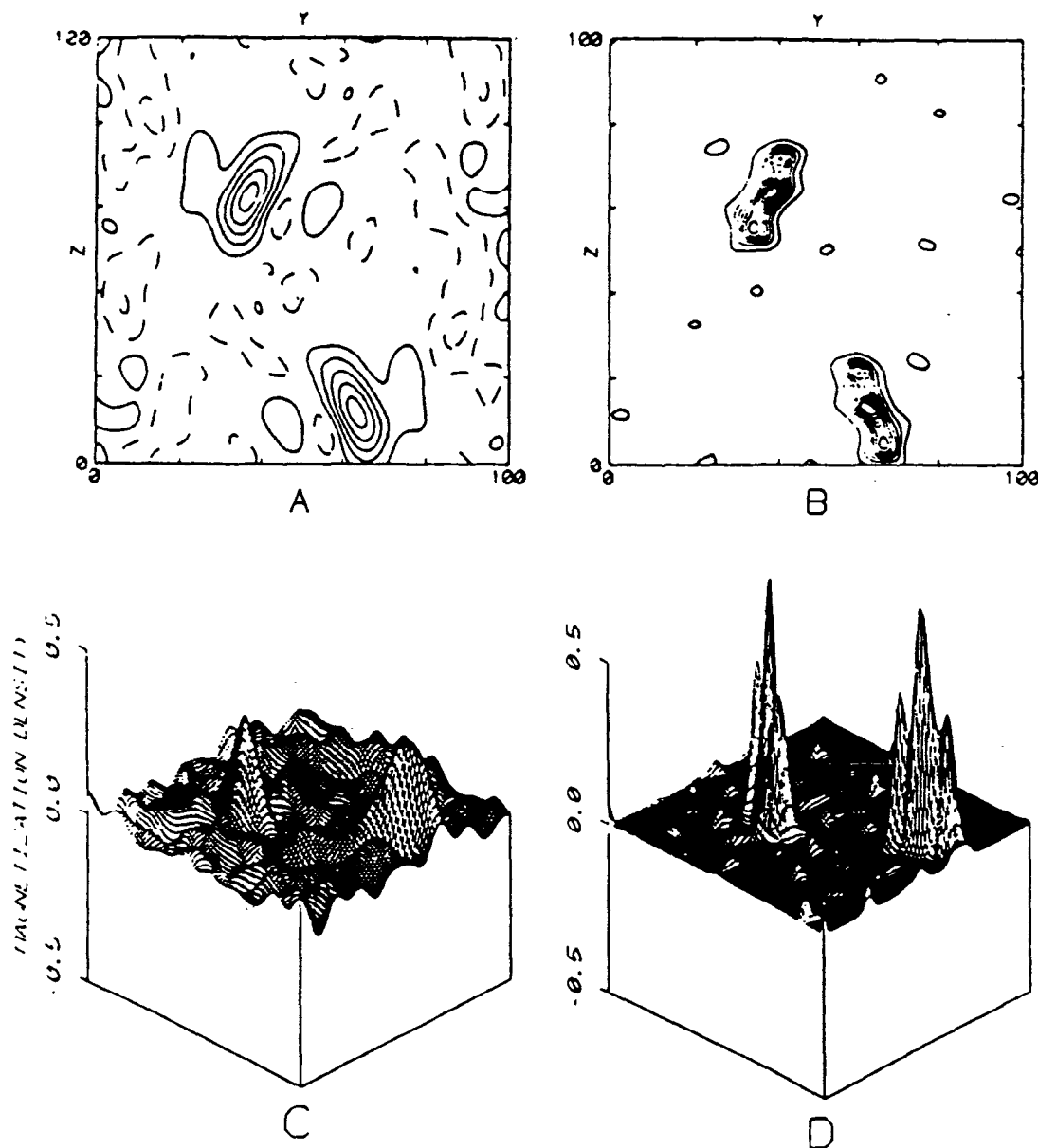
Fig. 13 A real data case: tanol suberate. The magnetisation density is projected along the $\bar{a}$ axis. The data consist of 69 independent Fourier components. The size of reconstructed image is 100*100 pixels.

Above, contour maps. A: Fourier, B: Maximum Entropy. The contour levels are the same in both A and B. The dotted lines refer to negative contours. Levels are $\pm.03, \pm.09, \pm.15, \pm.21 \ldots \mu_B/\text{Å}^2$. The Maximum Entropy reconstruction clearly resolves the density about the Oxygen and Nitrogen atoms, whereas the Fourier reconstruction does not.

Below, 3-D orthographic projections: C: Fourier, D: Maximum Entropy. The Maximum entropy reconstruction shows that the weight of the p_z orbital for the Oxygen is close to that of the p_z orbital for the Nitrogen. The larger peak results from the overlap of the projections of both orbitals.
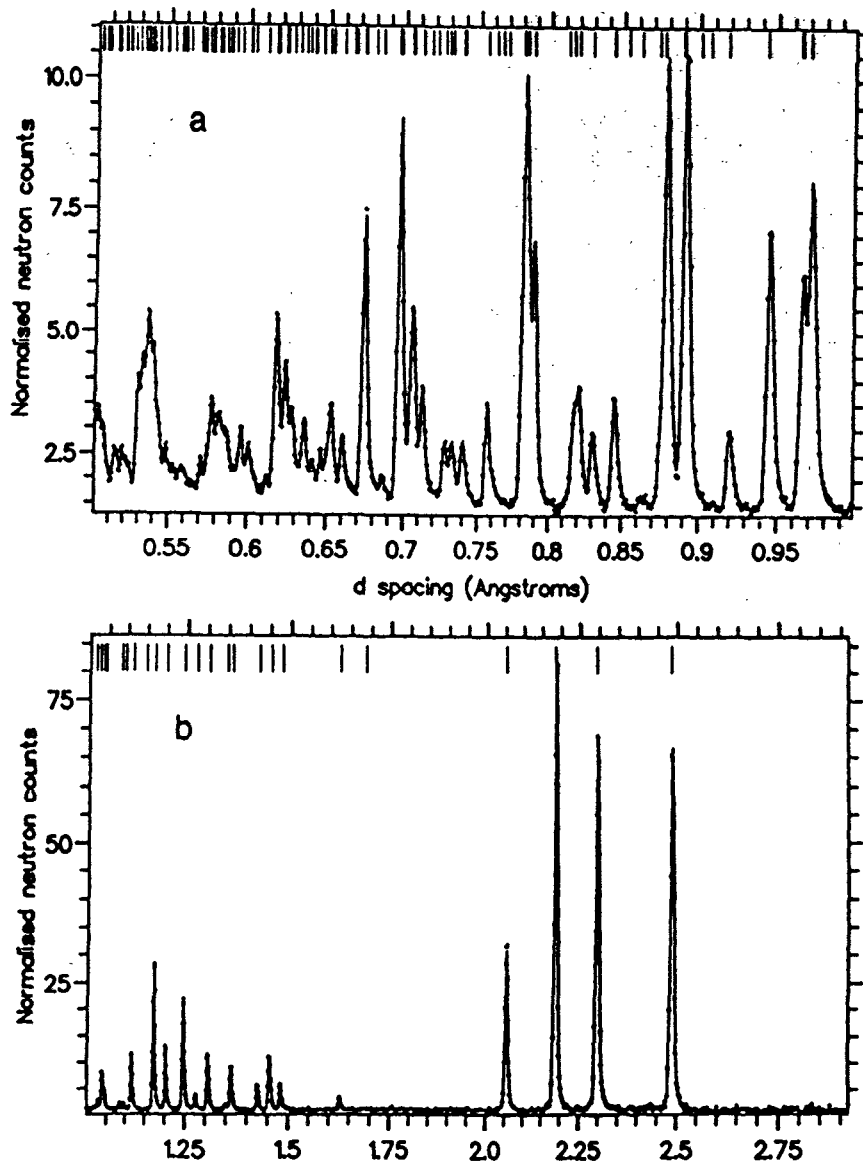
Figure 14

The observed (dots) and calculated (line) profiles for TiO_2 obtained using the POLARIS powder diffractometer at ISIS. The d-spacings range (a) from 0.5Å to 1Å and (b) from 1Å to 2.9Å. The tags mark the positions of Bragg reflections and clearly indicate the severe peak overlap particu' larly at short d-spacings.
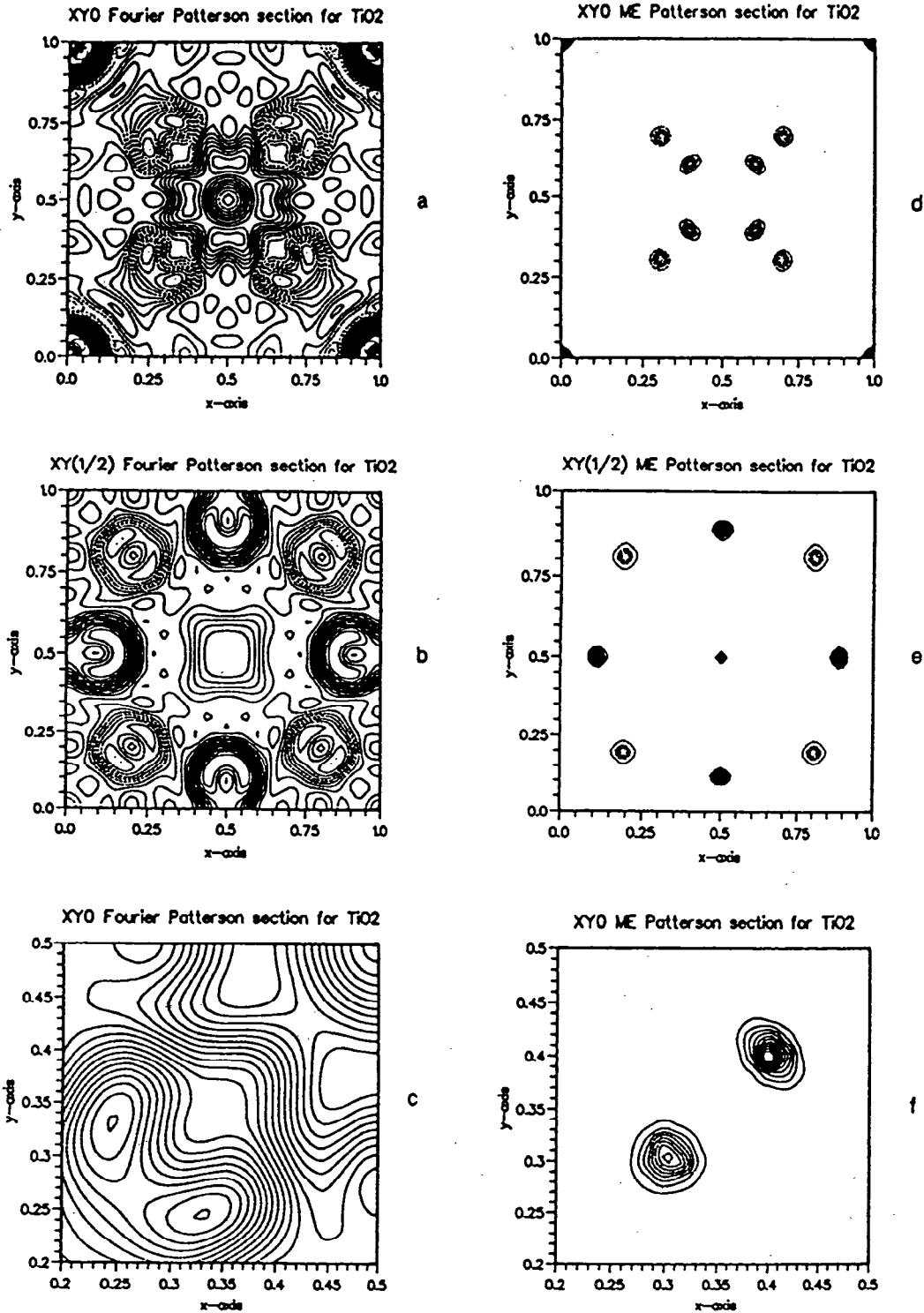
Figure 15

Figures 2a-c: Sections of the Patterson map synthesised by Fourier transformation of the squares of the structure factor magnitudes obtained from the Pawley-type profile refinement of TiO_2 and subsequent averaging of a sphere of diameter 0.5Å. The broad structural features indicate approximate vector positions but are severely distorted by misapportioning of intensities and truncation errors. The first two maps range over the full xy plane at (a) z=0 and (b) z = ½. Figure 2c is a magnification of Figure 2a with 0.2 < x < 0.5 and 0.2 < y < 0.5. Figures 2d-g: Sections of the Patterson map obtained by maximum entropy reconstruction from the observed clumps of Bragg intensities. The features are extremely sharp and are correctly located at interatomic vector positions. The map ranges in Figures 2d-g correspond to those of Figures 2a-c.
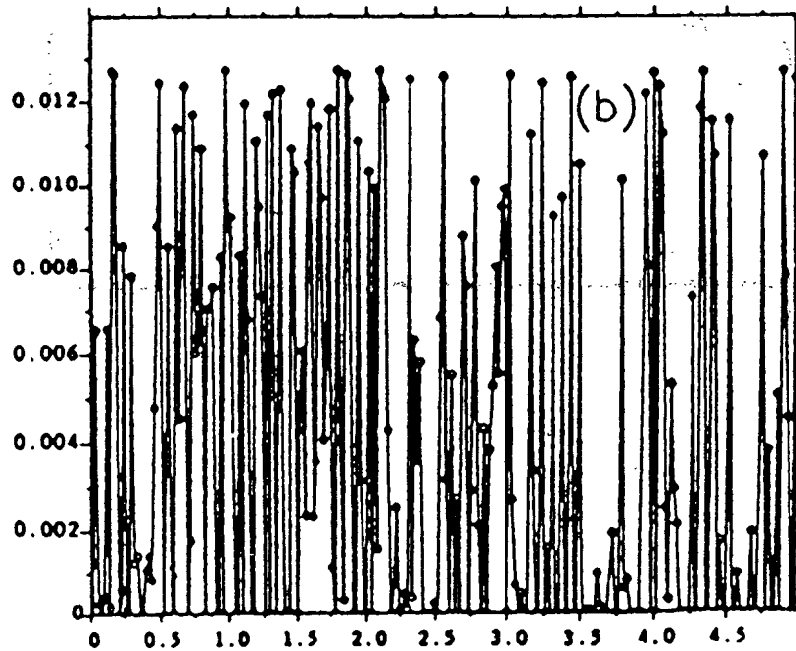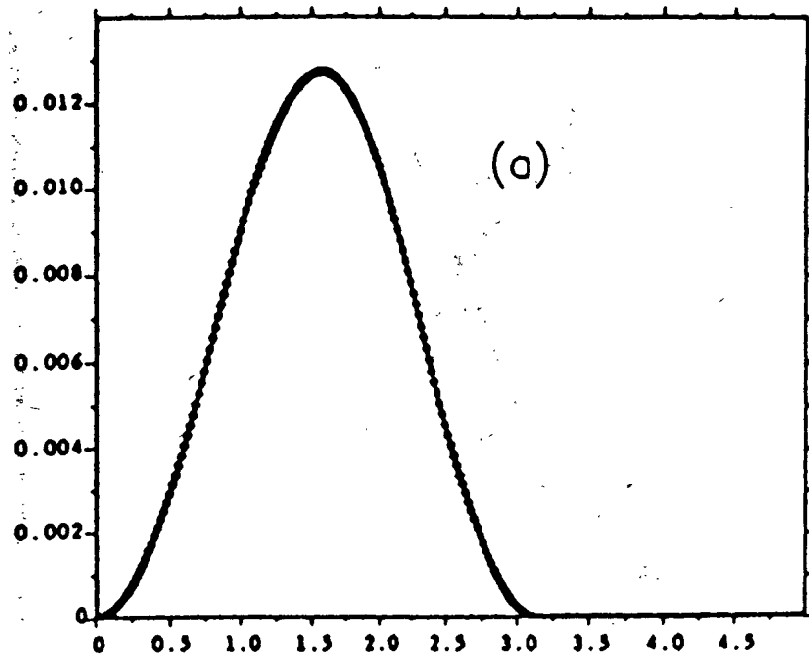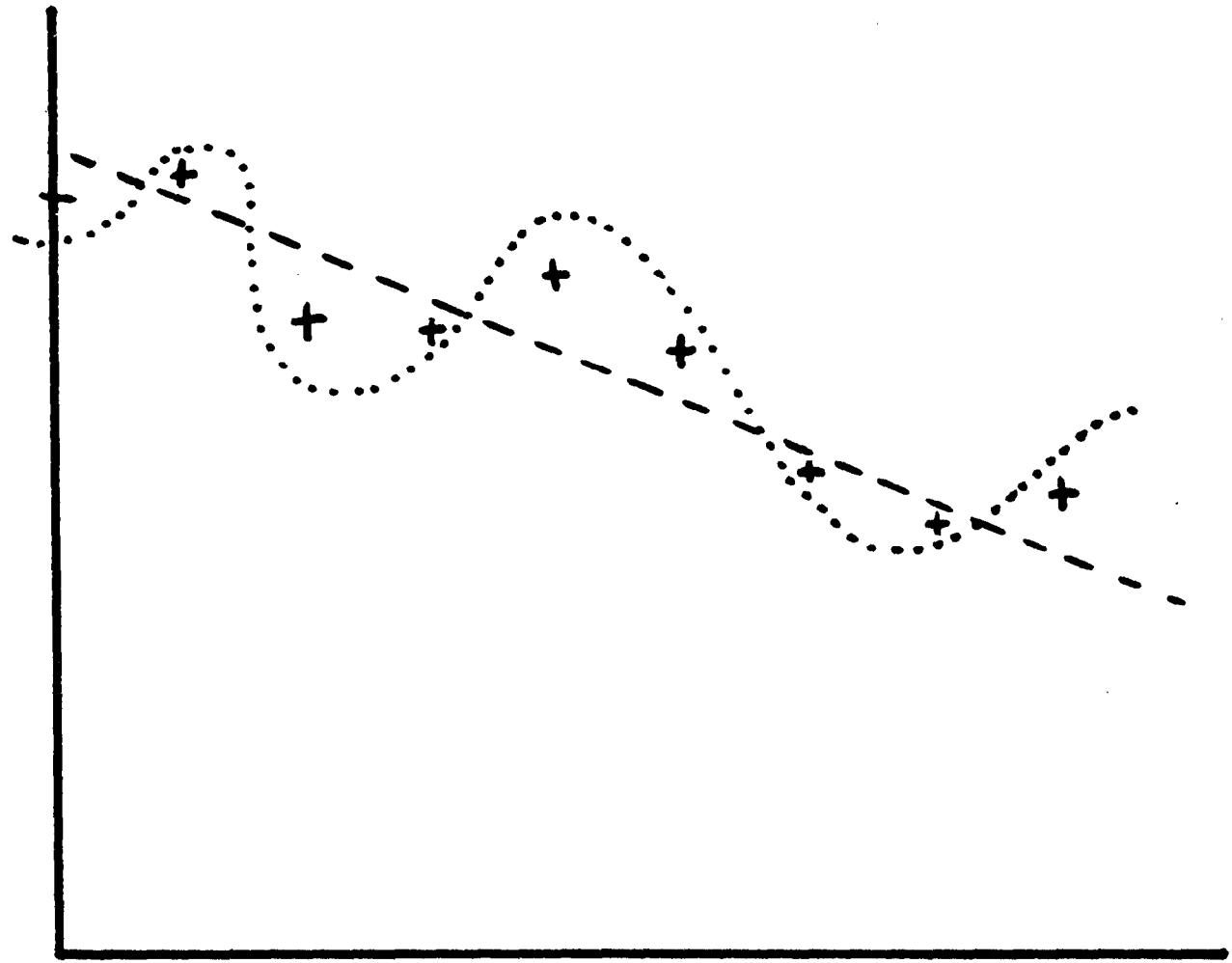
Fig 16

Fig 17

Q(J.B.Hayter): What are the implications of inelastic scattering in SANS experiments performed at pulsed sources? The Rennie-Ghosh experiments indicate that they may be significant, especially at short incident wavelength.

A(M.W.Johnson): Since T.O.F. LOQ experiments record the same Q information at different angles, there is the 'in principle' possibility of disentangling the elastic from the total scattering.